A kinetic analysis of the partial oxidation of C_3H_8 over a 2% Rh/Al_2O_3 catalyst in annular microreactor

Davide Pagani, Dario Livio, Alessandro Donazzi, Alessandra Beretta*, Gianpiero Groppi, Matteo Maestri, Enrico Tronconi

Laboratory of Catalysis and Catalytic Processes, Dipartimento di Energia, Politecnico di Milano, Piazza Leonardo da Vinci 32, 20133 Milano, Italy

ARTICLE INFO

ABSTRACT

In this paper, we report a detailed kinetic investigation of C_3H_8 catalytic partial oxidation (CPO) over a $Rh/\alpha-Al_2O_3$ catalyst. We applied an isothermal microreactor to collect kinetically relevant data with the aim of identifying the prevalent kinetic dependences and extending our C_1 molecular kinetic scheme to the description of the C_3H_8 CPO process. The kinetic study consisted of CPO and steam reforming tests with diluted feeding mixtures in a wide range of temperature, composition and space velocity. The experimental results showed that H_2 and CO are formed through consecutive steps of total oxidation and steam reforming of the fuel. The syngas composition is also affected by the water gas shift reaction, as well by the methanation of CO_x. In analogy with CH_4 CPO, the rate of total oxidation of C_3H_8 and the rate of steam reforming of C_3H_8 were found to be proportional to the concentration of fuel, but independent from the concentration of the co-reactant. The rate of the forward water gas shift reaction was found to be first order dependent on H_2O and independent from CO, while the rate of methanation was assumed to be proportional to H_2 partial pressure. A preliminary micro-kinetic analysis showed that C_3H_8 adsorption likely involves the formation of CH_x intermediates with $x \leq 2$.

© 2012 Elsevier B.V. All rights reserved.

1. Introduction

Small scale reformer designs are currently being developed for H_2 production in cogeneration systems based on fuel cells, but also for on-board applications. Herein hydrogen and hydrogen/CO_x mixtures are formed by catalytic conversion of a gaseous or liquid fuel in the presence of steam, CO_2 and/or O_2 [1–3]. Among the various processes and reactor solutions (externally heated reformers, exo–endo reformers, autothermal reformers), the catalytic partial oxidation (CPO) of hydrocarbon fuels in insulated short contact time reactors has several advantages: the flexibility to scale up and down, the fast light off, the resistance to extinction after load changes, high H_2 yields at millisecond contact times, the possibility of fully autothermal operation after light-off [4–9]. This is important in systems of a smaller scale than conventional hydrogen or syngas plants and particularly if restrictions on weight and/or volume are tight. The CPO process is based on the selective conversion of hydrocarbon and O_2 into CO and H_2 on metals (Ni, Pd, Pt, Rh), typically deposited in the form of a catalytic washcoat over high void fraction structures such as foams or honeycomb monoliths.

Recent research concerning the kinetics and mechanisms of the CPO process has been focused on methane for both fundamental

(the understanding of C—H bond activation on metals) and applicative scopes; natural gas is in fact the major feedstock for the production of hydrogen on nickel and noble metals-based catalysts [6,10–12]. However, the catalytic partial oxidation of C_{2+} hydrocarbons is also attractive for the small scale production of H_2. LPG (propane and butane) is the feedstock of choice for the delocalized production of hydrogen in remote areas, as an alternative to NG. Logistic fuels, such as gasoline, kerosene and diesel, are instead the available fuels for on-board hydrogen production. The use of C_{2+} fuels for H_2 production opens new technical challenges, such as the thermal behavior of the reactor (the adiabatic temperature rise of stoichiometric feed streams increases with increasing C-number of the alkane fuel), the interplay between surface and homogeneous reactions, the formation of coke and soot and, in general, the catalyst stability.

Schmidt et al. [13–17] have widely investigated the partial oxidation of gaseous, liquid, and solid hydrocarbon fuels to syngas at adiabatic temperatures ranging from 800 to 1200 °C using noble metal-coated monoliths at residence times between 10^{-3} and 10^{-2} s. Short contact time ceramic monoliths and foams were used as catalyst carriers and Rh was found to have superior performance in terms of H_2 yield and resistance to coke-formation.

Deutschmann et al. [18–20] combined experimental and simulation methods in the study of the catalytic partial oxidation of iso-octane over a rhodium coated monolithic catalyst. In particular, they investigated the effect of flow rate and C/O ratio on conversion,

H_2 yield, the formation of soot precursors and reactor heat losses. Very high hydrogen and carbon monoxide selectivity was found at stoichiometric conditions (C/O = 1), while at lean conditions total oxidation mainly occurred. At very rich conditions (C/O > 1), homogeneous chemical conversion in the gas-phase was responsible for the formation of by-products such as olefins that also have the potential for coke formation, which was observed experimentally and numerically. Deutschmann et al. [21] also performed an extensive study of steam reforming of C_1–C_4 alkanes over a Rh-based catalyst, showing that ethane, propane, and butane have almost identical conversion and selectivity as function of temperature and steam to carbon ratio.

Concerning the thermal behavior of the reformer, in recent studies on CH_4 and C_3H_8 CPO [22–25], we have shown that the high temperature levels reached in the reactor deactivate the catalyst even when noble metals are employed. The spatially resolved measurements and the model analysis of the axial concentration profiles confirm that the balance between the rate of the exothermic oxidation (fully limited by O_2 mass transfer) and the rate of endothermic steam reforming plays a pivotal role in determining the final temperature profile. On one side, we need to consider that for stoichiometric fuel/air mixtures, the inlet concentration of O_2 increases with increasing C-number of the alkane fuel, so that in the case of C_3H_8 CPO, the rate of heat release is larger than that of CH_4 CPO due to the higher O_2 concentration; on the other side, it was found that in the specific case of C_3H_8 CPO the rate of heat removal is slowed down because of the external diffusive resistances that affect the steam reforming of propane.

In this paper, we report a detailed kinetic investigation of C_3H_8 CPO over Rh/α-Al_2O_3 catalyst. An isothermal microreactor with annular configuration was applied to collect kinetically relevant data over a wide range of operating conditions. Aim of the work is to extend our C_1 molecular kinetic scheme in order to describe the C_3H_8 partial oxidation process. A preliminary micro-kinetic analysis was also addressed. Thus, while most of the experimental investigations concerning the CPO of C_{2+} hydrocarbons have focused on the performance of adiabatic reactors, the present study focuses on providing the pathways and the prevailing kinetic dependences of the surface reactions.

2. Experimental and modeling

2.1. Catalyst preparation

α-Al_2O_3 was used as a thermally stable support. It was obtained by calcination in air at 1100 °C for 10 h of commercial γ-Al_2O_3 (Puralox Sba-150, Sasol). Phase composition was verified by XRD, superficial area by BET analysis (Tristar Micromeritics) and pore size distribution by Hg porosimetry (Micromeritics AuotoPore IV). BET surface area amounted to about 9 m^2/g, with a pore volume of 0.2 cm^3/g. Rh(NO$_3$)$_3$ (a 14.68 wt.% solution in water, Chempur) was deposited onto α-Al_2O_3 via the incipient wetness technique. The impregnated support material was dried at 110 °C for 3 h. The catalytic powders were deposited in the form of thin layers (15–30 μm) on alumina tubular supports by a dip-coating standard procedure, described in detail elsewhere [26]. A slurry was prepared by adding catalyst powders to an acidic solution (HNO$_3$/powder = 1.7 mmol/g, H_2O/powder = 1.7 g/g) and it was ball-milled for 24 h; the alumina tubular support was coated on its terminal portion (2 cm from the sealed end) by dipping into the slurry and extracting at constant velocity; the coated tube was dried at 280 °C for 10 min (flash-drying) obtaining a well adhered catalyst layer. Rh loading of the catalyst (2%) was verified by atomic adsorption analysis of the flash-dried powders.

2.2. Testing apparatus

Reaction tests at high space velocity were carried out in a structured reactor with annular configuration. The reactor consists of an inner catalyst-coated ceramic tube, coaxially inserted into an outer quartz tube (I.D. 5 mm), giving rise to an annular duct through which the gas flows in laminar regime. The reactor design allowed to operate at very high GHSV (10^6–10^7 l(NTP)/kg$_{cat}$/h) with negligible pressure drops. Given the thermal equilibrium across the section of the ceramic tube, the temperature on the catalyst surface can be measured by sliding a thermocouple (K-type) inside the alumina tube itself [27]. Notably, the effective dissipation of the heat of reaction by radiation from the ceramic tube to the oven inner wall allows to maintain low axial temperature gradients, as better illustrated in the following. In all the figures, data are reported as a function of the catalyst average temperature. This was calculated as an arithmetic average of the single measurements taken each 2 mm along the length of the layer (2 cm). Continuous axial profiles were reconstructed by polynomial interpolation of the axially resolved measurements and were used for data modeling. Oven temperatures were measured by a second K-type thermocouple sliding in a mullite tube which was placed along the heating wall. The feed gases were supplied by high pressure cylinders through pressure reducing stages and low pressure mass flow controllers (BROOKS smart 5850S).

Steam was produced by feeding a stoichiometric mixture of H_2 and O_2 diluted in N_2 in an independent reactor placed upstream of the annular reactor; it consisted of a quartz tube, where 5% Pt-αAl_2O_3 powders were packed on top of a layer of quartz wool. This solution allowed a good control of H_2O flow that could be kept constant during the test. GC analysis always confirmed the absence of any H_2 and O_2 slip from the steam generator. Downstream lines were heated up to 120 °C to prevent water condensation.

A micro-GC (3000 A, Agilent Technologies) was used to analyze the inlet and the outlet gas compositions using N_2 as an internal standard. In all the runs, the balances of the converted moles of C, H and O closed within ±5%, and in most cases ±3%. A scheme of the testing rig is shown in Fig. 1.

2.3. Operating conditions and measurement procedure

All the tests were performed at atmospheric pressure. A typical run consisted of steady-state measurements at varying oven temperatures from 300 up to 850 °C, with step-wise increments of 50 °C. At each temperature, conversions and selectivities were measured by repeated analyses and they showed stable values within 15–20 min. Prior to the kinetic tests, the catalyst underwent a standard conditioning procedure, developed and discussed in previous studies [28]. Periodically, CPO standard tests were performed with C_3H_8 in order to verify possible loss of activity. Operating conditions of these runs were 1% C_3H_8 (v/v), O_2/C = 0.56, N_2 to balance and GHSV of 2×10^6 l(NTP)/kg$_{cat}$/h.

2.4. 1D mathematical model of the annular reactor and thermodynamic analysis

The experimental results were quantitatively analyzed by a 1D heterogeneous model of the reactor, which incorporates a molecular kinetic scheme. It consists of our previously developed C_1 molecular scheme [29,30], which was extended to account for C_3H_8 conversion on Rh. Governing equations, boundary conditions and transport correlations are reported in dimensionless form in Table 1. The same model was discussed and applied in previous works [29,30], herein we note that intra-phase mass transfer limitations were described using generalized efficiency factors (Eqs. (4)–(6)) for O_2, CH_4 and C_3H_8; ηO_2 was calculated on the basis of
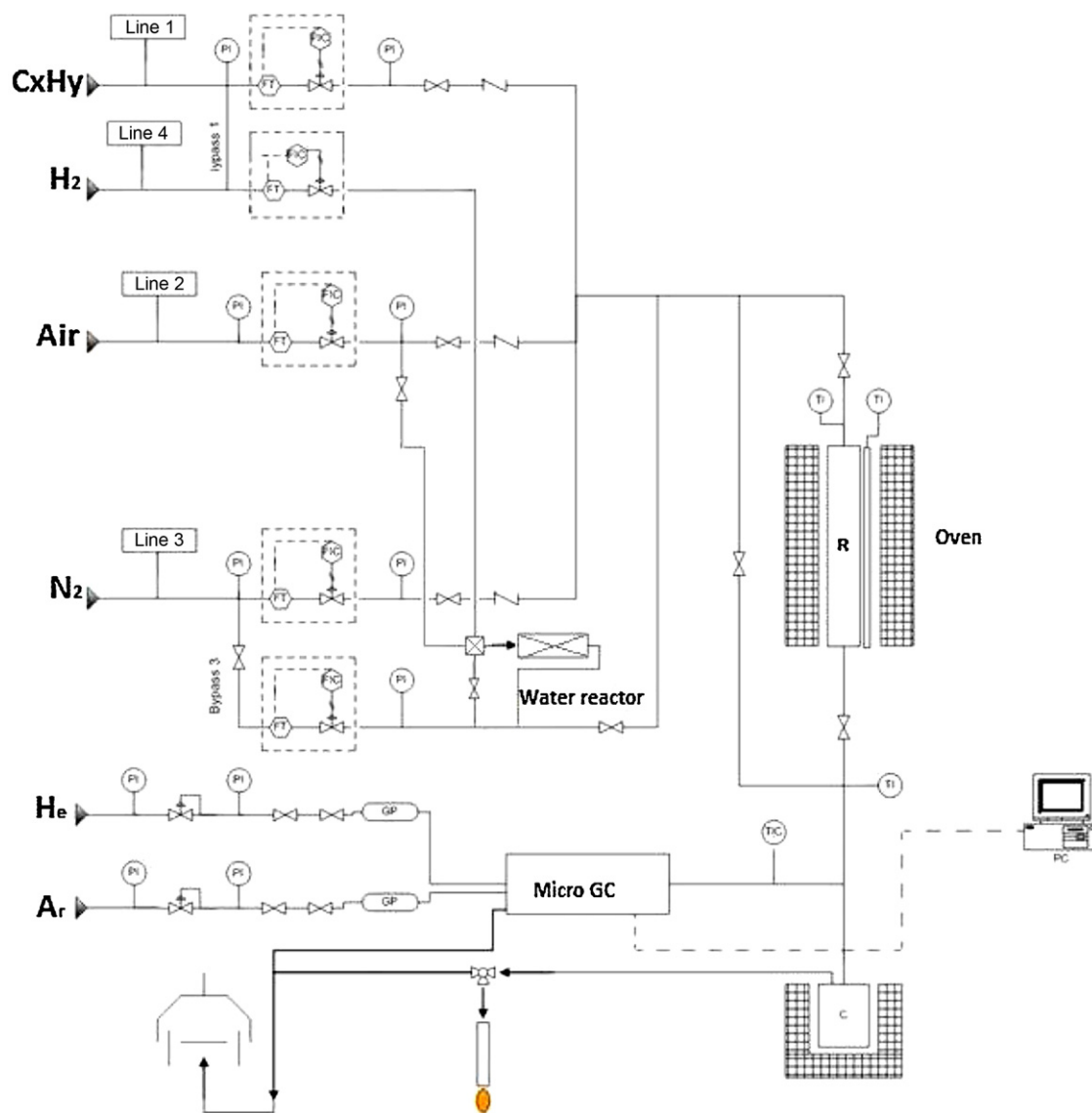
Fig. 1. Apparatus scheme.

the overall rate of O_2 consuming reactions (oxidation of CH_4, C_3H_8, H_2 and CO), while ηCH_4 and ηC_3H_8 represents the effectiveness factors for the steam reforming of CH_4 and C_3H_8, respectively.

Thermodynamic calculations have been performed using the Stanjan code [31] including C_3H_8, C_3H_6, C_2H_4, CO, CO_2, H_2, H_2O, O_2 and H_2. CH_4 was only included to calculate CH_4 equilibrium concentration while C formation was never considered.

3. Experimental results

3.1. CPO – effects of temperature and GHSV

C_3H_8 partial oxidation tests were performed with diluted feed streams ($C_3H_8 = 1\%$, $O_2/C = 0.56$, N_2 to balance) in the temperature range 300–850 °C at varying gas space velocity from 2×10^6 to 6×10^6 l(NTP)/kg_{cat}/h. The molar fractions of reactants and products are plotted against the catalyst average temperature in Figs. 2 and 3. Deep oxidation of C_3H_8 started at temperature around 300–350 °C and up to 400–450 °C, H_2O and CO_2 were the only detectable products. At about 400 °C the C_3H_8 conversion curves showed a change of slope, caused by the transition from the deep

oxidation regime to the combined oxidation plus reforming regime. In fact, when O_2 conversion was complete, a decrease of CO_2 and H_2O molar fractions was observed, while CO and H_2 production increased steadily with increasing temperature and C_3H_8 consumption, until reaching of the equilibrium composition. At increasing GHSV, the conversion of C_3H_8 and O_2 decreased and the temperatures for complete O_2 conversion grew, while syngas production was "delayed" at higher temperatures. The production of syngas was accompanied by the formation of methane (Fig. 3), whose concentration passed through a maximum at about 600 °C, and then decreased according to the thermodynamic equilibrium. Above 700 °C small amounts of C_2H_4, C_3H_6 were also detected; CH_4, C_2H_4 and C_3H_6 molar fractions increased with increasing temperature and GHSV: the amount of by-products measured was originated by gas-phase reactions that occurred into the empty volumes of the annular reactor and were comparable with the amounts measured in blank tests of oxidative pyrolysis (not reported for brevity). The fact that gas-phase products were visible only at the highest space velocity suggests that the oxidative pyrolysis did not occur upstream from the catalyst layer, but likely involved the residual fraction of C_3H_8, which did not react on the catalyst surface

Table 1
Model equations of the reactor.

Mass balance equation, bulk phase (*i*th, species):

$$(1)\, Pe_{m,i} \cdot \frac{dF_i^*}{dz^*} = -\frac{4}{1+(1/R^*)} \cdot Sh_{loc_i} \cdot (x_i^B - x_i^W) \cdot \frac{F_{TOT}}{F_{TOT}^0}$$

Continuity equation, catalyst phase (*i*th, species):

$$(2)\, Sh_{loc_i} \cdot (x_i^B - x_i^W) = \sum_{j=1}^{NR} \upsilon_{i,j} \cdot \alpha_i \cdot R_j$$

Mass transfer coefficient:

$$(3)\, Sh_{loc_i} = Sh_{inf} + 6.874 \cdot e^{-71.2 \cdot z_{Sh_i}} \cdot (1000 \cdot z_{Sh_i})^{-0.35}$$

Generalized internal efficiency:

$$(4)\, \eta_{O_2}^\infty = \frac{\sqrt{2}}{\delta_L \cdot r_{O_2} \cdot (C_{O_2}^S)} \cdot \sqrt{\int_0^{C_{O_2}^S} D_{eff,O_2} \cdot r_{O_2}(C) \cdot dC}, \quad \Phi_{O_2} = \frac{1}{\eta_{O_2}^\infty}, \quad \eta_{O_2} = \frac{\tanh(\Phi_{O_2})}{\Phi_{O_2}}$$

$$(5)\, \eta_{CH_4}^\infty = \frac{\sqrt{2}}{\delta_L \cdot r_{CH_4} \cdot (C_{CH_4}^S)} \cdot \sqrt{\int_{C_{CH_4}^{eq}}^{C_{CH_4}^S} D_{eff,CH_4} \cdot r_{CH_4}(C) \cdot dC}, \quad \Phi_{CH_4} = \frac{1}{\eta_{CH_4}^\infty}, \quad \eta_{CH_4} = \frac{\tanh(\Phi_{CH_4})}{\Phi_{CH_4}}$$

$$(6)\, \eta_{C_3H_8}^\infty = \frac{\sqrt{2}}{\delta_L \cdot r_{C_3H_8} \cdot (C_{C_3H_8}^S)} \cdot \sqrt{\int_{C_{C_3H_8}^{eq}}^{C_{C_3H_8}^S} D_{eff,C_3H_8} \cdot r_{C_3H_8}(C) \cdot dC}, \quad \Phi_{C_3H_8} = \frac{1}{\eta_{C_3H_8}^\infty}, \quad \eta_{C_3H_8} = \frac{\tanh(\Phi_{C_3H_8})}{\Phi_{C_3H_8}}$$

Effective diffusivity coefficient:

$$(7)\, D_{eff_i} = \varepsilon_M^2 \cdot D_{M,i} + \frac{\varepsilon_\mu^2 \cdot (1+3 \cdot \varepsilon_M)}{1-\varepsilon_M} \cdot D_{\mu_i}$$

Note. Index $i = C_3H_8$, CH_4, O_2, CO, CO_2, H_2, H_2O.

due to the short contact time and the presence of interphase mass transfer limitations. Because of the onset of gas phase reactions, under these high flow rate conditions, H_2, H_2O and CO_x were not equilibrated according to the absolute thermodynamic equilibria.

Fig. 4A reports the measured axial temperature profiles, referred to the oven wall temperature profiles. The temperature difference between the catalyst and the oven grew significantly at increasing O_2 conversion from 300 to 400 °C. At higher temperatures, the gap with the oven wall temperature decreased progressively, with increasing synthesis gas selectivity; a hot spot formed at the beginning of the catalyst layer, followed by a decreasing temperature trend. Despite the important heat dispersion from the annular catalyst layer, some residual temperature gradients were present. Fig. 4B also reports the difference between maximum and minimum temperature along the catalytic layer. In most experiments this amounted to about 15 °C.

Within this and other previous investigations, we have observed that the obtainment of almost isothermal conditions is strictly controlled by the degree of dilution of the reacting mixture and by the total flow rate. At increasing concentration of the reactants as well as at increasing flow rate, the differences between maximum and minimum temperatures along the catalyst layer become more and more important. When T-axial gradients exceed 5 °C/cm, the kinetic analysis is performed by accounting for the axial temperature profiles, obtained by polynomial interpolation of the thermocouple measurements.

3.2. CPO – effect of N_2 dilution

CPO tests were carried out by keeping constant the O_2/C ratio at 0.56 and GHSV at 2×10^6 l(NTP)/kg$_{cat}$/h and varying the concentration of C_3H_8 from 1 to 4%. Fig. 5 reports reactants conversion and product distribution against the average catalyst temperature. The increase of the reactants concentration caused a decrease of both C_3H_8 and O_2 conversion; for instance, the temperature of the complete consumption of O_2 grew from 380 to 430 °C. The process, thus, showed a global reaction order lower than 1. The productivity

of H_2 and CO_x increased with increasing inlet reactants concentration and, especially at the highest temperatures, were close to thermodynamic equilibrium. Only in the test with the highest C_3H_8 concentration, the molar fractions of H_2 and CO were significantly lower than the equilibrium values up to 600 °C; however, a partial deactivation of the catalyst occurred in this run. A subsequent reference experiment at 1% C_3H_8 concentration showed in fact that in the reforming zone ($T > 400$ °C) the loss in the catalytic activity amounted to 10–15%. No additional runs were thus performed with the same tube.

CH_4 formation was also observed (Fig. 6A); as general trends, the measured outlet molar fraction of methane increased with temperature and with C_3H_8 concentration. At high temperatures ($T > 600$ °C) the molar fraction of CH_4 decreased in line with the thermodynamic equilibrium. It is worthy to note that, in spite of a factor of 2 between the inlet concentration of C_3H_8 in the data sets with symbols (■) and (●) (Fig. 6A, curves corresponding to 2% and 4% propane inlet concentration), the production of methane at 450–550 °C kept almost unchanged. In the same temperature range also the mole fraction of CO and H_2 were comparable in the two runs because of the above mentioned partial loss of activity in the test at 4% propane concentration. This peculiar similarity supported the hypothesis that the formation of CH_4 originated from syngas, rather than from catalytic cracking of C_3H_8. Additional experiments with $CO_x/H_2/N_2$ feed mixtures were performed and confirmed the presence of a methanation route, whose mechanism and kinetics are presently under investigation. Above 600 °C, C_2H_4 and C_3H_6 were formed in small amount (not reported for brevity) only in the tests at the highest reactants concentration, where the fuel conversion was incomplete.

3.3. CPO – effect of O_2 concentration

Tests were carried out keeping C_3H_8 inlet fraction at 1% (v/v), GHSV at 2×10^6 l(NTP)/kg$_{cat}$/h and varying O_2 concentrations from 1.68%, to 2.25% and 3% (v/v). The conversion of the reactants and the molar fractions of the products are plotted against average
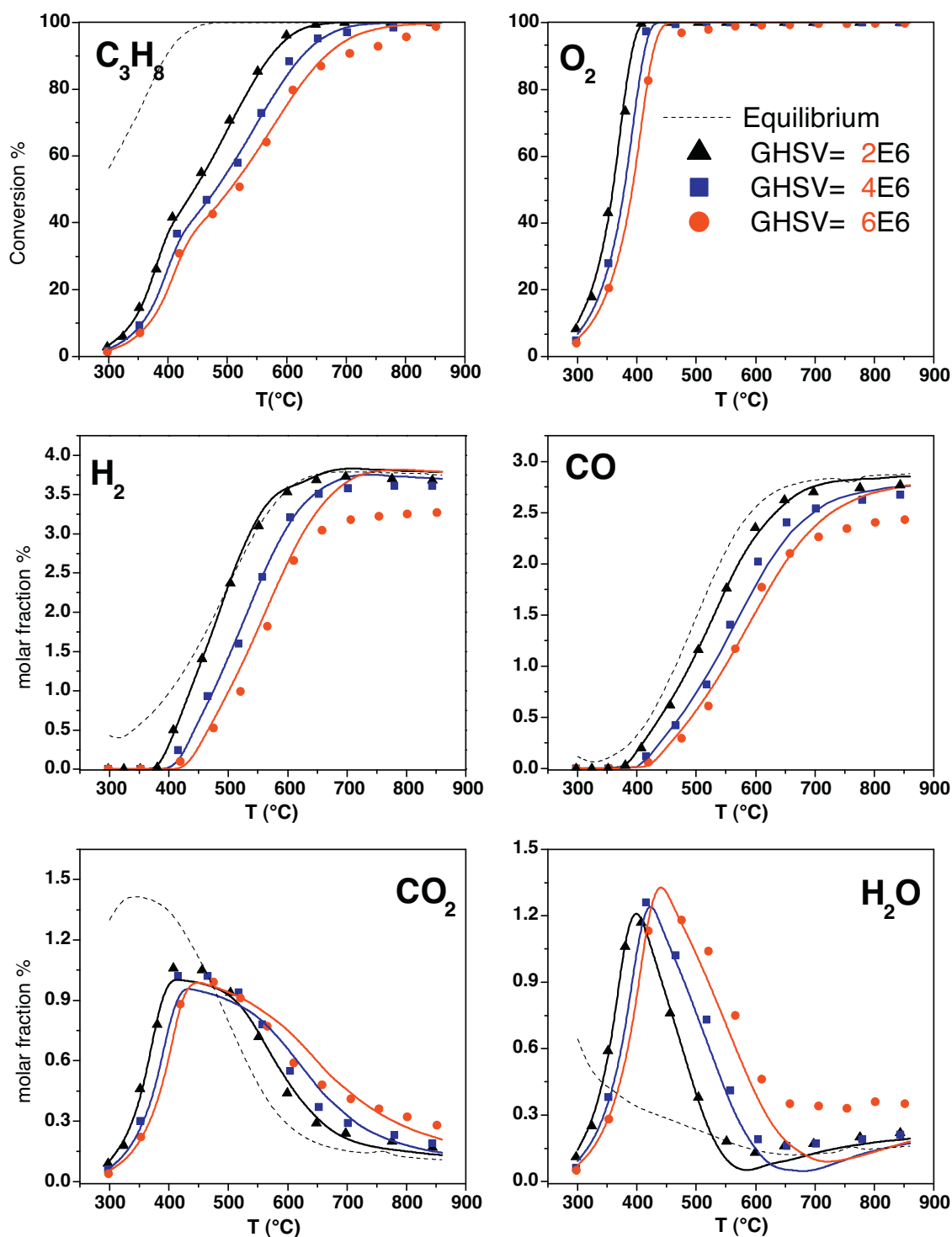
Fig. 2. Effect of GHSV on reactants and products molar fractions. Experimental (symbols) and calculated (solid lines) fractions are reported. (▲) GHSV = 2×10^6 l(NTP)/kg$_{cat}$/h; (■) GHSV = 4×10^6 l(NTP)/kg$_{cat}$/h; (●) GHSV = 6×10^6 l(NTP)/kg$_{cat}$/h; (dashed line) equilibrium. Feed composition: C_3H_8 = 1% (v/v), O_2/C = 0.56, N_2 to balance; atmospheric pressure.

catalyst temperatures in Fig. 7. At low temperature, the C_3H_8 conversion was not affected by the change of oxygen concentration, whereas the O_2 conversion decreased with increasing O_2 inlet concentration. The increase of oxygen inlet concentration led to an extension of the deep oxidation zone at progressively higher temperatures; in fact the temperature thresholds for complete O_2 conversion and for maximum production of H_2O were shifted at higher values. Moreover, the fraction of C_3H_8 that reacted with

oxygen to CO_2 and H_2O grew with increasing O_2 concentration, thus reducing the residual amount of fuel available for reforming reactions. Therefore, with increasing O_2 concentration, H_2 and CO production was delayed at higher temperature, and syngas selectivity decreased. On increasing the O_2 concentration a maximum in H_2 molar fraction (and selectivity) appears at 600 °C, while CO molar fraction monotonically increases according to WGS/RWGS equilibration.
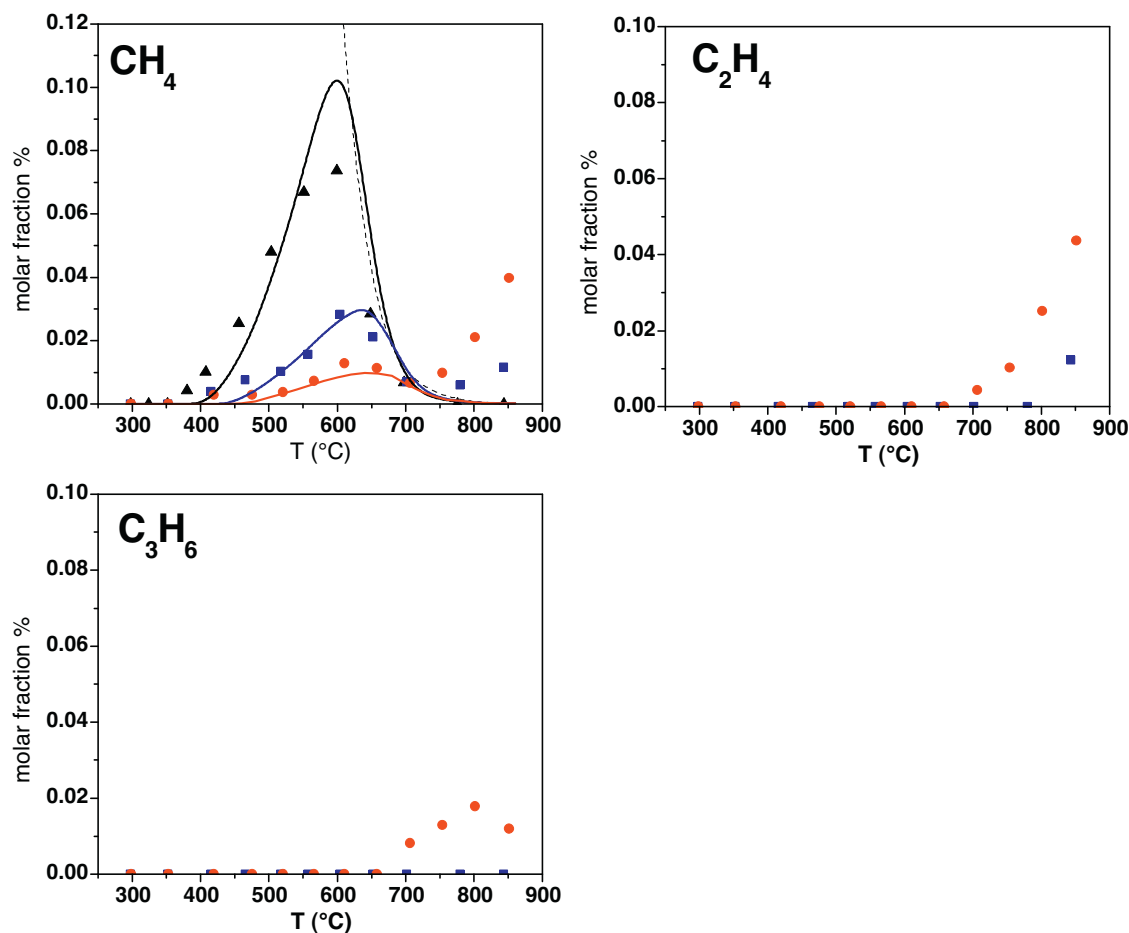
Fig. 3. Effect of GHSV and temperature on hydrocarbon side-products molar fractions. Experimental (symbols) fractions are reported. (▲) GHSV = 2×10^6 l(NTP)/kg$_{cat}$/h; (■) GHSV = 4×10^6 l(NTP)/kg$_{cat}$/h; (●) GHSV = 6×10^6 l(NTP)/kg$_{cat}$/h; (dashed line) equilibrium. Feed composition: C_3H_8 = 1% (v/v), O_2/C = 0.56, N_2 to balance; atmospheric pressure.

Additionally, the increase of O_2 molar fraction caused a reduction of CH_4 formation (data are reported in Fig. 6B), consistently with the hypothesis that methanation and not catalytic cracking is responsible for CH_4 production at low-medium temperature.

3.4. CPO – effect of C_3H_8 concentration

Tests were carried out keeping O_2 inlet fraction at 3% (v/v), GHSV at 2×10^6 l(NTP)/kg$_{cat}$/h and varying the concentration of C_3H_8
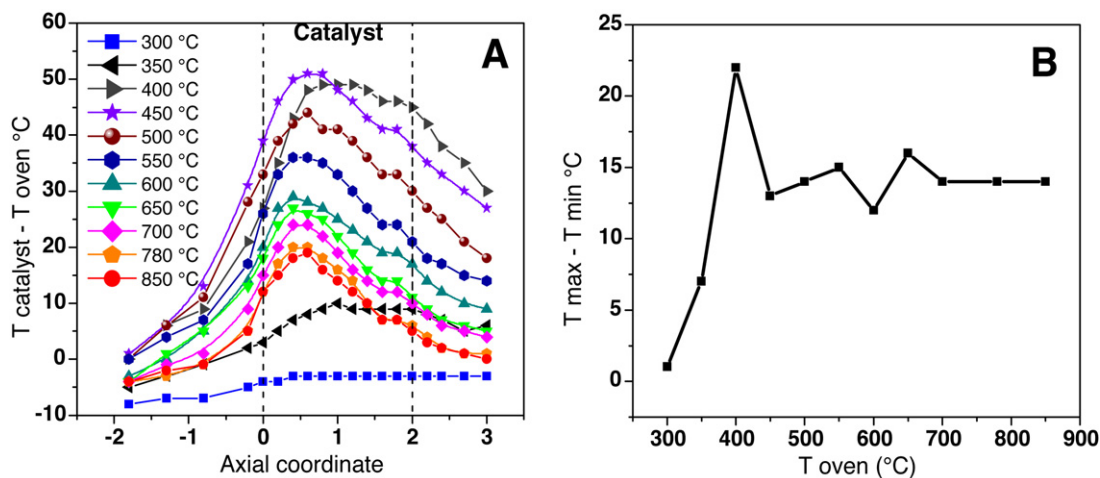

Fig. 4. (A) Temperature profile on the catalyst layer at varying the oven set temperature. Operating conditions: GHSV = 2×10^6 l(NTP)/kg$_{cat}$/h, C_3H_8 = 1% (v/v), O_2/C = 0.56, N_2 to balance, atmospheric pressure. (B) Maximum axial gradients on the catalyst layer as a function of the average catalyst temperature. Operating conditions: GHSV = 2×10^6 l(NTP)/kg$_{cat}$/h, C_3H_8 = 1% (v/v), O_2/C = 0.56, N_2 to balance, atmospheric pressure.
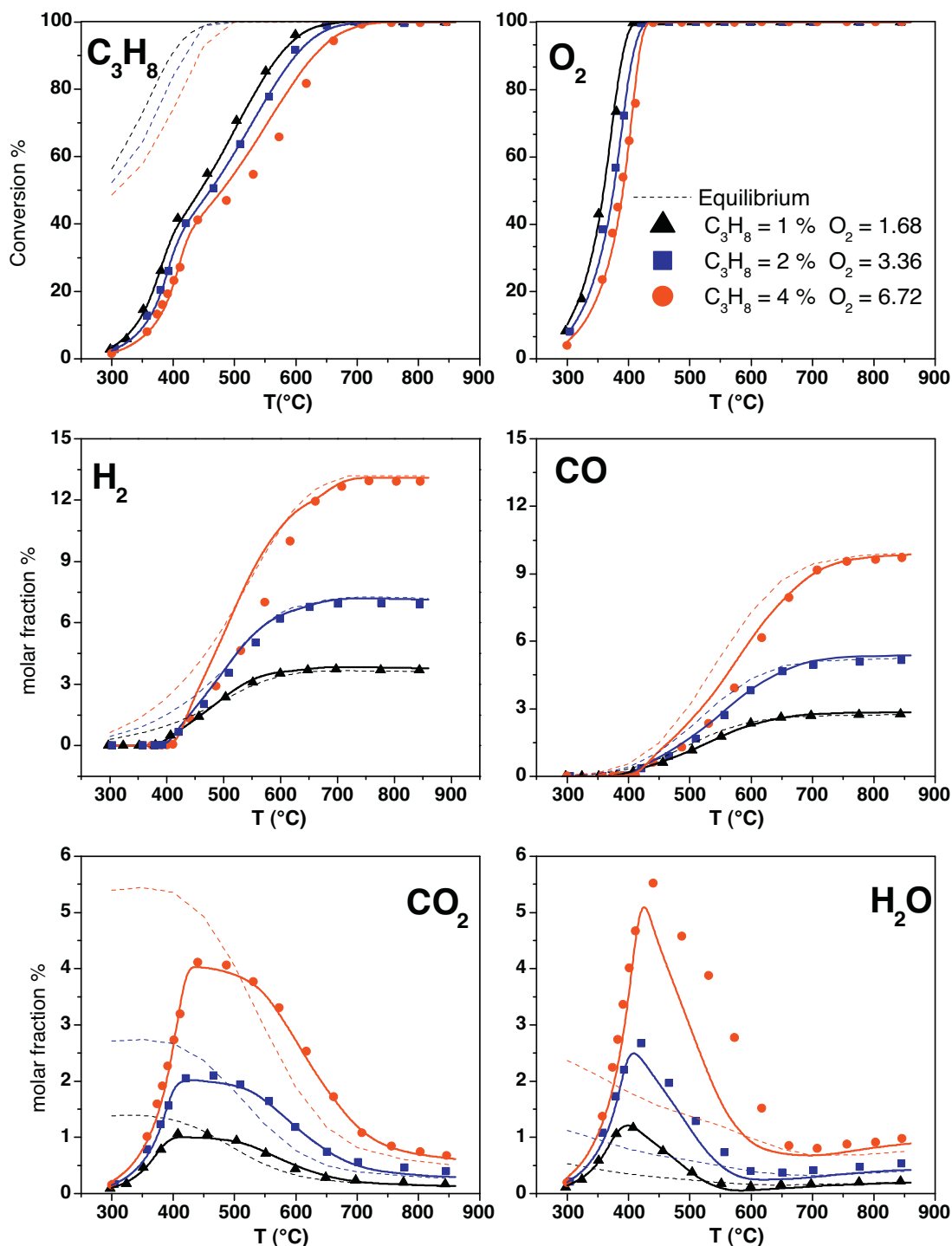
Fig. 5. Effect of dilution on reactants and products molar fractions. Experimental (symbols) and calculated (solid lines) fractions are reported. Feed composition: (▲) C_3H_8 = 1% (■) C_3H_8 = 2% (●) C_3H_8 = 4%; O_2/C = 0.56, N_2 to balance. GHSV = 2×10^6 l(NTP)/kg$_{cat}$/h, atmospheric pressure.

from 1%, to 1.35% and 1.8% (v/v). The conversion of the reactants and the molar fraction of the products are plotted as a function of the average catalyst temperature in Fig. 8. At low temperature, C_3H_8 conversion slightly decreased at increasing C_3H_8 concentration; at the same time, the productivity of H_2O and CO_2 increased only moderately. The conversion of O_2 also increased in the same direction. Above the temperature of complete O_2 conversion, the fuel fraction available for the reforming reactions grew with increasing C_3H_8 inlet concentration, consequently, H_2 and CO molar fractions increased accompanied by a higher consumption of H_2O and CO_2.

Also the formation of CH_4 (as reported in Fig. 8C) followed the trend of syngas productivity.

3.5. SR – effect of C_3H_8 concentration

Tests of steam reforming were carried out at GHSV at 2×10^6 l(NTP)/kg$_{cat}$/h in the temperature range 300–850 °C, varying the concentration of C_3H_8 from 0.5% to 0.8% while the amount of H_2O was kept constant at 3%. The conversion of the reactants and the molar fraction of the products are plotted as a function of
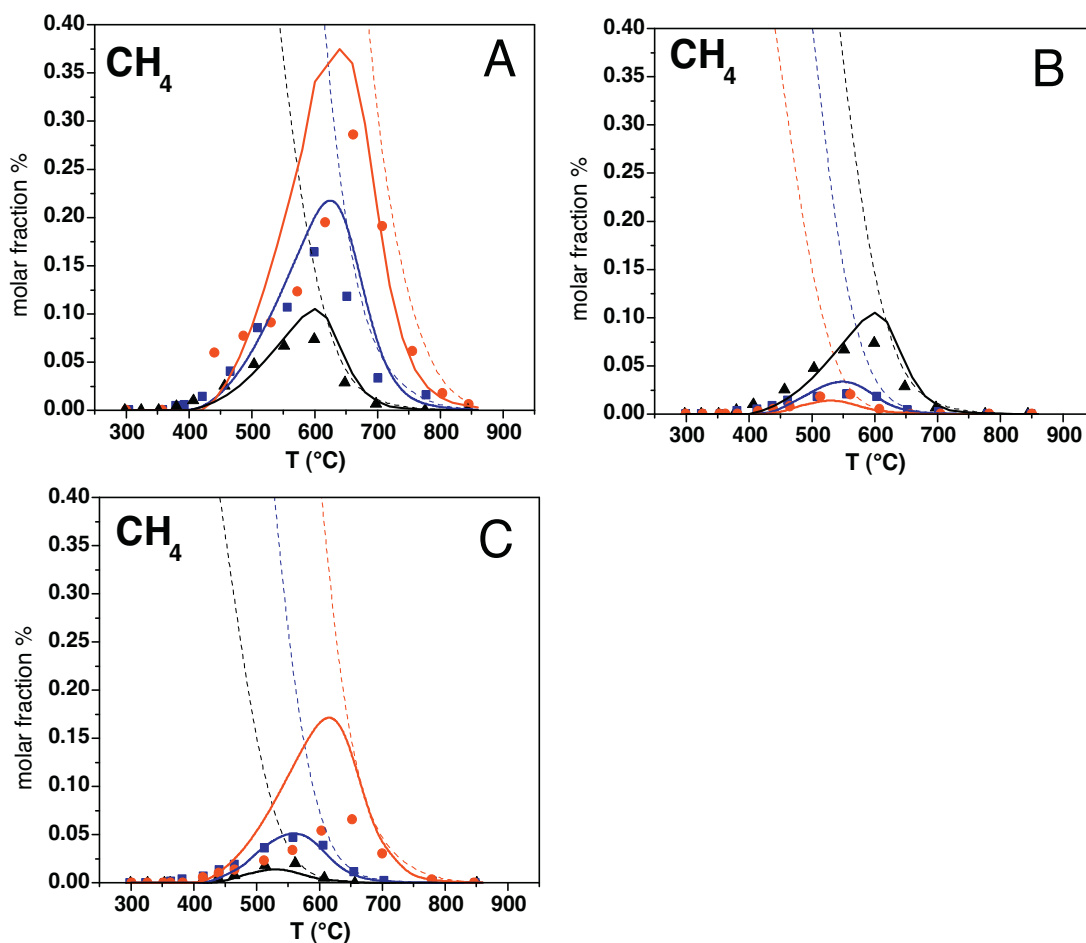
Fig. 6. Methane molar fractions. (A) Feed composition: (▲) $C_3H_8 = 1\%$ (■) $C_3H_8 = 2\%$ (●) $C_3H_8 = 4\%$; $O_2/C = 0.56$, N_2 to balance; GHSV = 2×10^6 l(NTP)/kg$_{cat}$/h, atmospheric pressure. (B) Feed composition: (▲) $O_2 = 1.68\%$ (■) $O_2 = 2.25\%$ (●) $O_2 = 3\%$; $C_3H_8 = 1\%$, N_2 to balance; GHSV = 2×10^6 l(NTP)/kg$_{cat}$/h, atmospheric pressure. (C) Feed composition: (▲) $C_3H_8 = 1.0\%$ (■) $C_3H_8 = 1.35\%$ (●) $C_3H_8 = 1.8\%$; $O_2 = 3.0\%$, N_2 to balance; GHSV = 2×10^6 l(NTP)/kg$_{cat}$/h, atmospheric pressure.

the average catalyst temperature in Fig. 9. The conversion of C_3H_8 and H_2O progressively increased with temperature and reached the equilibrium value at about 800 °C. Upon increasing C_3H_8 inlet concentration, the conversion of H_2O increased in the whole temperature range; instead, the measurements of C_3H_8 conversion showed similar values up to 450 °C, while a small negative effect of the fuel partial pressure was found at higher temperatures. The CO and H_2 production increased steadily with increasing temperature and C_3H_8 consumption, until reaching of the equilibrium composition. The production of CO_2 passed through a maximum according to the equilibrium of the water gas shift reaction, which is approached above 650 °C. A complete overlap of CO_2 molar fraction curves at increasing C_3H_8 concentration could be observed up to 500 °C.

Also in SR tests, the production of syngas was accompanied by the formation of methane, whose concentration passed through a maximum at about 600 °C, and then decreased according to thermodynamic equilibrium.

4. Kinetic analysis

Data were analyzed with the aim of formulating "simple" rate expressions, capable to describe the reaction scheme and the product distribution that were observed both in CPO and SR of C_3H_8. In view of reactor design purposes, the availability of a molecular kinetic scheme with a reduced set of parameters can be of great practical interest. In addition to this, the identification of prevailing

kinetic dependences is a preliminary step before addressing a more detailed micro-kinetic modeling of the process (a similar hierarchical multiscale approach was successfully applied for developing a C_1 micro-kinetic scheme on Rh [32]). Also, the quantification of kinetics through the definition of molecular rate expressions provides the means for comparing the chemical behavior of different fuels, such as CH_4 and C_3H_8. Several similarities are apparent between the C_3H_8/O_2 reacting system and the CH_4/O_2 reacting system. Similarly to CH_4, the experiments showed that also C_3H_8 is fully oxidized to CO_2 and H_2O when O_2 is present on the catalyst surface, while synthesis gas was observed at temperatures higher than those necessary for complete conversion of O_2. The partial oxidation of C_3H_8 to CO and H_2 appears then as an indirect process of oxidation and steam reforming, as CH_4 partial oxidation over Rh is, wherein the possible role of H_2 and CO post combustions cannot be ruled out. The data showed that the products distribution respected the equilibrium of water gas shift under many conditions; WGS and its reverse are then important reactions. The formation of CH_4 at low-medium temperatures accompanied the formation of syngas, which makes necessary the inclusion of a methanation reaction in the kinetic scheme. Only at the highest temperatures, the activation of side gas-phase cracking reactions became significant with production of CH_4, C_2H_4 and C_3H_6. The heterogeneous path was instead assumed to be responsible for the observed kinetic effects. These were described by assuming the indirect kinetic scheme (consisting of propane oxidation and steam reforming, WGS/RWGS, CO and H_2 post-combustion and
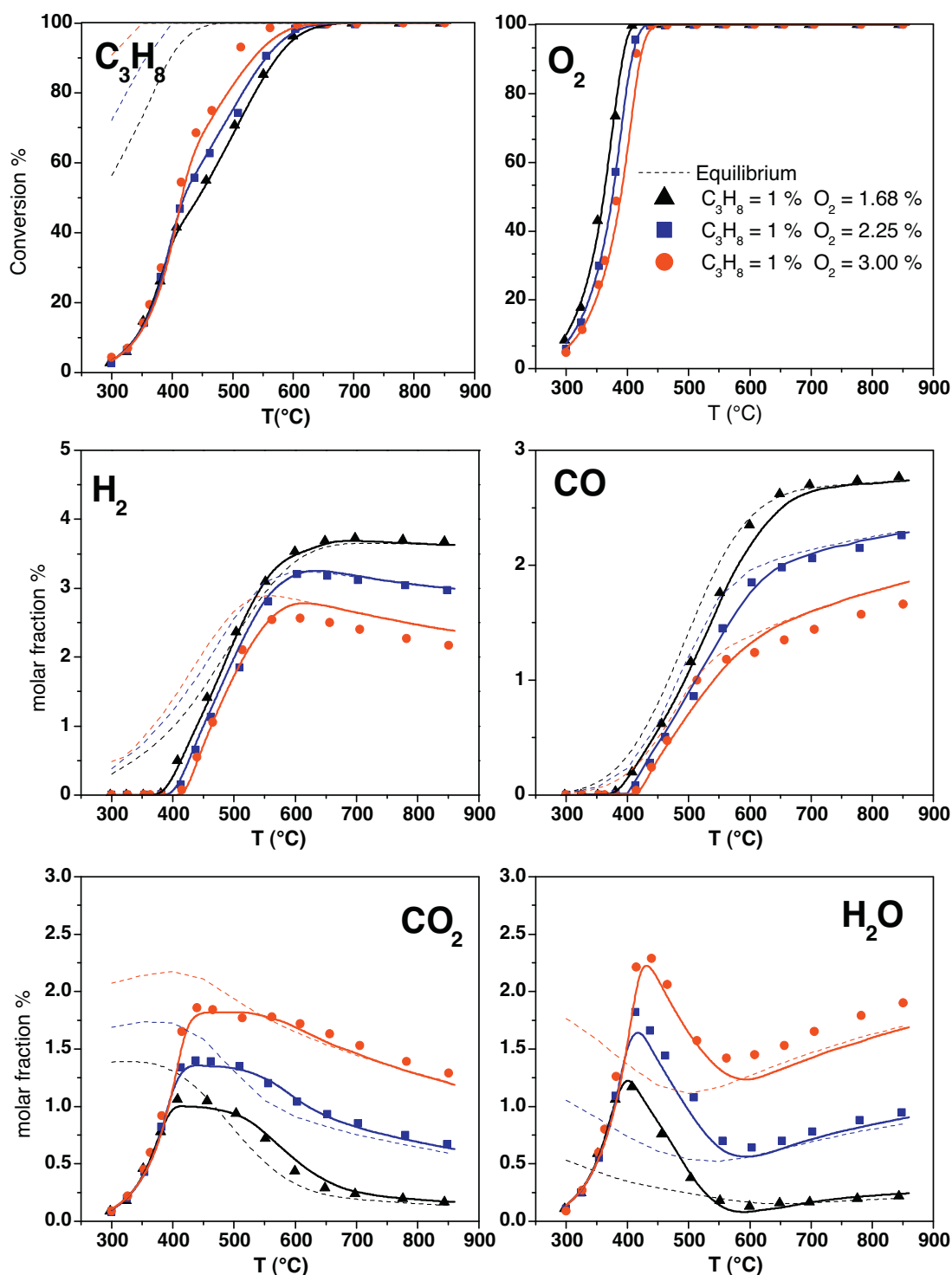
Fig. 7. Effect of O_2 fed on reactants and products molar fractions. Experimental (symbols) and calculated (solid lines) fractions are reported. Feed composition: (▲) $O_2 = 1.68\%$ (■) $O_2 = 2.25\%$ (●) $O_2 = 3\%$; $C_3H_8 = 1\%$, N_2 to balance; GHSV $= 2 \times 10^6$ l(NTP)/kg$_{cat}$/h, atmospheric pressure.

methanation) and the molecular rate expressions, as reported in Table 2. The kinetic scheme was adapted to the experimental data by applying the reactor model above discussed, which includes and filters the effect of inter- and intra-phase mass transfer resistances. The adequacy of the model is supported by the very satisfactory accordance between symbols and solid lines (the calculated trends) in Figs. 2, 3 and 5–9. The scheme extends our previous kinetic scheme of CH_4 partial oxidation [29,30]. It is worthy to note that the parameters marked with the asterisk * were estimated

in a previous study on methane [29], while all the remaining ones were independently estimated in this work. Rate expressions and kinetic parameters are illustrated in the following. The estimates of parameters are listed in Table 2 and expressed in the modified Arrhenius form $k(T) = k(T_{ref}) \exp(-E_{act}/R(1/T - 1/T_{ref}))$, more suitable to minimize the correlation between pre-exponentials and activation energies. A common reference temperature T_{ref} of 600 °C is used to compare the parameters in Table 2.
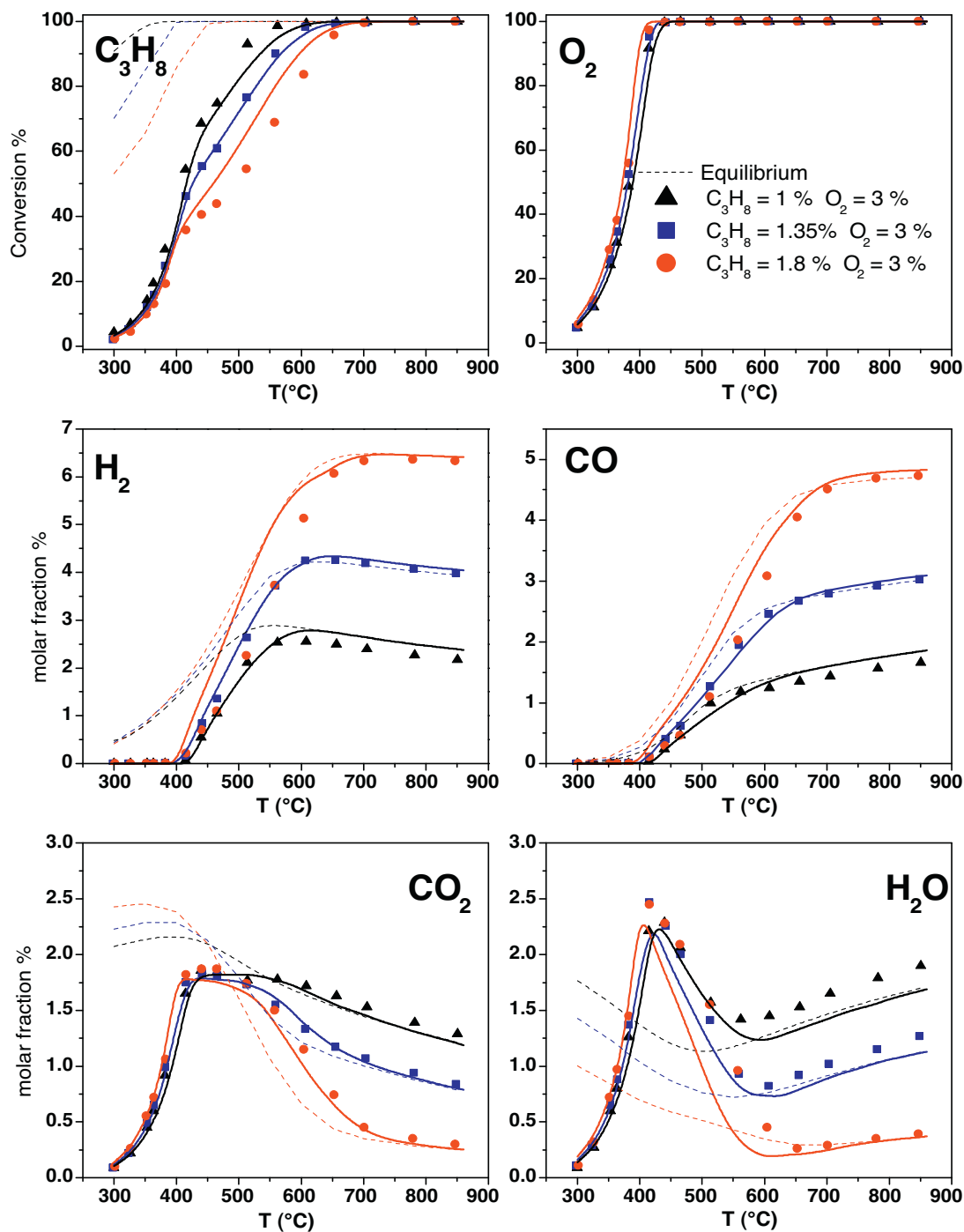
Fig. 8. Effect of C_3H_8 fed on reactants and products molar fractions. Experimental (symbols) and calculated (solid lines) fractions are reported. Feed composition: (▲) $C_3H_8 = 1.0\%$ (■) $C_3H_8 = 1.35\%$ (●) $C_3H_8 = 1.8\%$; $O_2 = 3.0\%$, N_2 to balance; GHSV $= 2 \times 10^6$ l(NTP)/kg$_{cat}$/h atmospheric pressure.

4.1. Total oxidation of C_3H_8

All the CPO tests characterized by incomplete conversion of O_2 (i.e. at temperature below 400 °C) were treated as C_3H_8 total oxidation data. Thus, they were used to tune the kinetic expression of C_3H_8 deep oxidation. The experiments at varying O_2 concentration (Fig. 7) indicated that the rate of C_3H_8 combustion was independent from O_2 concentration; this is in line with the picture a fully oxygen-saturated surface. The experiments at varying C_3H_8 concentration (Fig. 8) indicated that the rate of C_3H_8 combustion had a positive dependence from the fuel concentration; however, when the concentration of the reactants was increased (Fig. 5), a decrease

of conversion was observed, thus revealing an overall kinetic order lower than unity. On the basis of these and of previous independent observations [29], the following expression was proposed:

$$r_{Ox_{C_3H_8}} = \frac{k_{Ox_{C_3H_8}} \cdot P_{C_3H_8}}{1 + K_{ads_{H_2O}} \cdot P_{H_2O}} \cdot \sigma_{O_2} \tag{8}$$

It should be noted that a similar dependence was adopted to describe the complete oxidation of methane in CH_4 CPO [29]:

$$r_{Ox_{CH_4}} = \frac{k_{Ox_{CH_4}} \cdot P_{CH_4}}{1 + K_{ads_{H_2O}} \cdot P_{H_2O}} \cdot \sigma_{O_2} \tag{9}$$
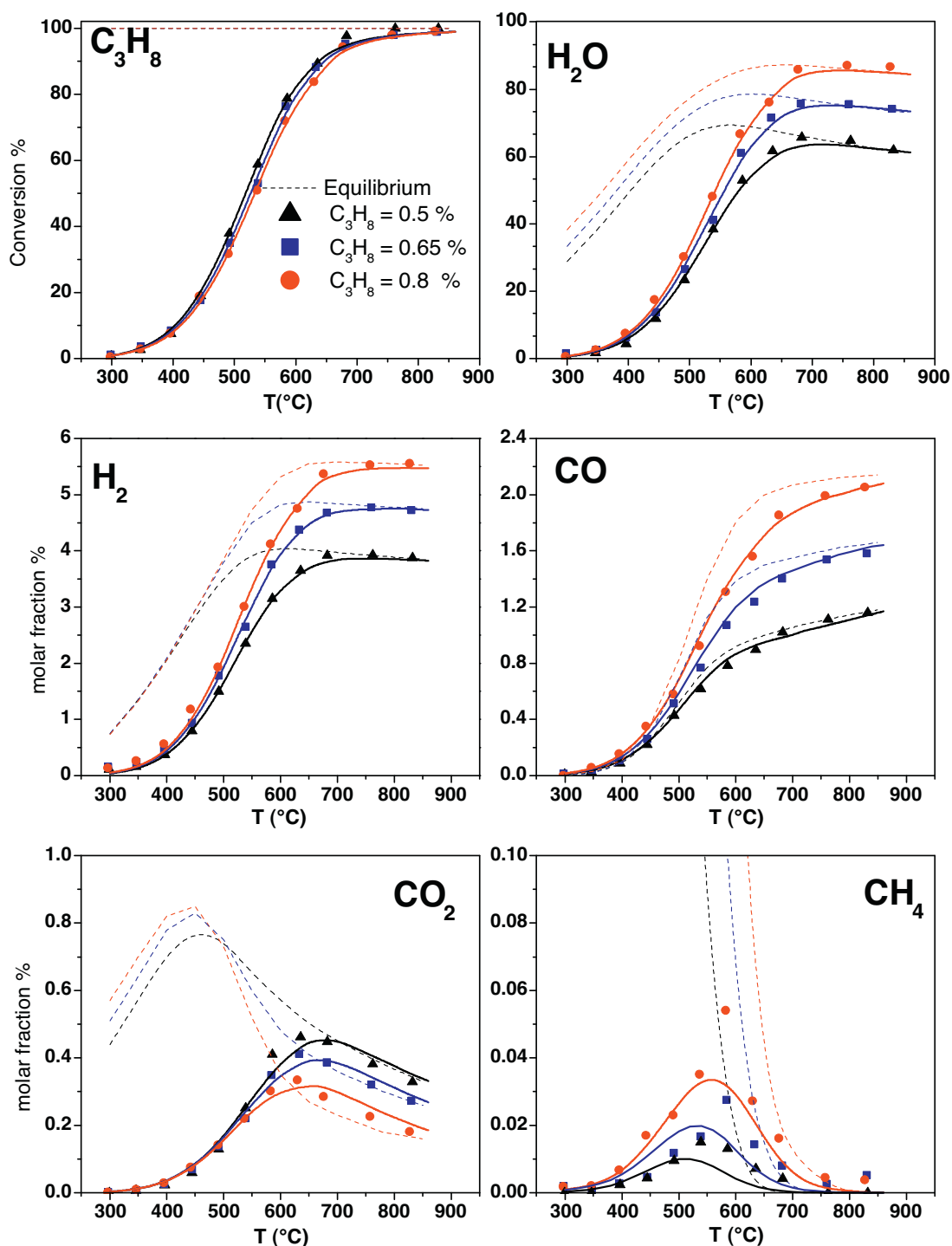
Fig. 9. Effect of C_3H_8 fed on reactants and products molar fractions. Experimental (symbols) and calculated (solid lines) fractions are reported. Feed composition: (▲) $C_3H_8 = 0.5\%$ (■) $C_3H_8 = 0.65\%$ (●) $C_3H_8 = 0.8\%$; $H_2O = 3.0\%$, N_2 to balance; GHSV $= 2 \times 10^6$ l(NTP)/kg$_{cat}$/h, atmospheric pressure.

with:

$$\sigma_i = \frac{P_i}{P_i + 10^{-6}} \qquad (10)$$

Considering the independence of the C_3H_8 total oxidation rate from O_2, the σ_{O_2} term is necessary to correctly describe the situation of absence of the co-reactant (that is, $r_{OX_i} = 0$ at $P_{O_2} = 0$). The minimum tolerance value which guarantees the numerical convergence in the simulations is 10^{-6} atm.

Eq. (8) includes an inhibition term due to the competitive adsorption of water. Such a term was introduced to explain the decrease of C_3H_8 conversion with increasing reactants concentration. The total combustion products, CO_2 and H_2O, could inhibit the reaction; we did not collect direct pieces of evidence, however our previous work [29] showed that in the presence of H_2O, the activation of CH_4 in the low temperature range was delayed and that H_2O has a much stronger inhibiting effect than CO_2.

These results are qualitatively in line with the kinetics of CH_4 activation, the analogies between oxidation of CH_4 and C_3H_8

Table 2
Kinetic scheme and parameter estimates.

Reaction	Rate equation [mol/(g_{cat} s)]	$k_i^{873\,K}$[mol/(atm g_{cat} s)]	E_{act} [kJ/mol]
C_3H_8 total oxidation	$r_{Ox\_C_3H_8} = \frac{k_{Ox\_C_3H_8} \cdot P_{C_3H_8}}{1+K_{ads\_H_2O} \cdot P_{H_2O}} \cdot \sigma_{O_2}$		
$C_3H_8 + 5O_2 \rightarrow 3CO_2 + 4H_2O$		2.500×10^{-1}	80
C_3H_8 steam reforming	$r_{SR\_C_3H_8} = \frac{k_{SR\_C_3H_8} \cdot P_{C_3H_8} \cdot (1-\eta_{SR\_C_3H_8})}{1+K_{ads\_CO} \cdot P_{CO} + K_{ads\_O_2} \cdot P_{O_2}} \cdot \sigma_{H_2O}$		
$C_3H_8 + 3H_2O \leftrightarrow 3CO + 7H_2$		2.486×10^{-1}	85
CH_4 total oxidation	$r_{Ox\_CH_4} = \frac{k_{Ox\_CH_4} \cdot P_{CH_4}}{1+K_{ads\_H_2O} \cdot P_{H_2O}} \cdot \sigma_{O_2}$		
$CH_4 + 2O_2 \rightarrow CO_2 + 2H_2O$		$1.030 \times 10^{-1\,a}$	92[a]
CH_4 steam reforming	$r_{SR\_CH_4} = \frac{k_{SR\_CH_4} \cdot P_{CH_4} \cdot (1-\eta_{SR\_CH_4})}{1+K_{ads\_CO} \cdot P_{CO} + K_{ads\_O_2} \cdot P_{O_2}} \cdot \sigma_{H_2O}$		
$CH_4 + H_2O \leftrightarrow CO + 3H_2$		$1.027 \times 10^{-1\,a}$	92[a]
Direct water gas shift	$r_{WGS} = k_{WGS} \cdot P_{H_2O} \cdot (1-\eta_{WGS}) \cdot \sigma_{CO}$		
$CO + H_2O \rightarrow CO_2 + H_2$		6.831×10^{-3}	75
Reverse water gas shift	$r_{WGS} = k_{RWGS} \cdot P_{CO_2} \cdot (1-\eta_{RWGS}) \cdot \sigma_{H_2}$		
$H_2O + CO \rightarrow CO_2 + H_2$		$1.277 \times 10^{-2\,a}$	62[a]
Methanation	$r_{Met} = k_{Met} \cdot P_{H_2} \cdot (1-\eta_{Met}) \cdot \sigma_{CO}$		
$CO + 3H_2 \rightarrow H_2O + CH_4$		1.500×10^{-3}	30
H_2 oxidation	$r_{Ox\_H_2} = k_{Ox\_H_2} \cdot P_{H_2} \cdot \sigma_{O_2}$		
$H_2 + 1/2O_2 \rightarrow H_2O$		$2.666 \times 10^{3\,a}$	62[a]
CO oxidation	$r_{Ox\_CO} = k_{Ox\_CO} \cdot P_{CO} \cdot \sigma_{O_2}$		
$CO + 1/2O_2 \rightarrow CO_2$		$1.937 \times 10^{1\,a}$	76[a]

Surface adsorption	$k_i^{873\,K}$[atm^{-1}]	ΔH_{ads} [kJ/mol]
O_2	5.461[a]	−73[a]
H_2O	8.974	−57
CO	$2.114 \times 10^{2\,a}$	−37[a]

[a] Donazzi et al. [29].

suggest that the kinetic dependencies are direct consequences of surface coverage and hydrocarbon reactivity. Both CH_4 and C_3H_8 adsorb weakly in competition with oxygen giving O^* coverages close to. Recently, Iglesia et al. [33,34] provided a rigorous mechanistic interpretation of CH_4–O_2 and C_2H_6–O_2 reactions on supported Pt clusters, based on kinetic and isotopic data obtained under strict kinetic control, and from DFT calculations. They found that CH_4 and C_2H_6 oxidation in oxygen-saturated Pt surfaces lead to rates that are first-order in reductant (CH_4 or C_2H_6) pressure and independent of O_2 pressure.

The activation energy estimated for C_3H_8 oxidation amounts to 80 kJ/mol, lower than that estimated for methane (92 kJ/mol); also the intrinsic rate constant at 600 °C resulted nearly 2.5 times larger that of methane. Such higher reactivity is likely associated to the difference in the C—H bond strength.

4.2. Steam reforming of C_3H_8

Both the steam reforming data and all the CPO data at complete O_2 conversion are informative on the kinetics of C_3H_8 activation with H_2O. The results of the SR experiments at low fuel conversion (Fig. 9) showed that the intrinsic rate is first-order with respect to the concentration of C_3H_8 and comparable with the rate of oxidation. The high temperatures CPO experiments (Figs. 2 and 7) showed that the activation of steam reforming was delayed by the presence of O_2. Also, a term of inhibition due to the absorption of CO was introduced to explain the global reaction order lower than 1 observed at high fuel conversion both in the CPO and in the SR tests (Figs. 5 and 9). The following rate expression is thus proposed:

$$r_{SR_{C_3H_8}} = \frac{k_{SR_{C_3H_8}} \cdot P_{C_3H_8} \cdot (1 - \eta_{SR_{C_3H_8}})}{1 + K_{ads_{CO}} \cdot P_{CO} + K_{ads_{O_2}} \cdot P_{O_2}} \cdot \sigma_{H_2O} \qquad (11)$$

The kinetic parameters for CO and O_2 adsorption are the same as previously considered in methane steam reforming:

$$r_{SR_{CH_4}} = \frac{k_{SR_{CH_4}} \cdot P_{CH_4} \cdot (1 - \eta_{SR_{CH_4}})}{1 + K_{ads_{CO}} \cdot P_{CO} + K_{ads_{O_2}} \cdot P_{O_2}} \cdot \sigma_{H_2O} \qquad (12)$$

The thermodynamic constraint was respected by introduction of the term $(1 - \eta_{SR})$, wherein η_{SR} is the ratio of the experimental reaction quotient $K_{P,SR}$ and the thermodynamic equilibrium constant $K_{EQ,SR}$. The term σ_{H_2O} is defined according to Eq. (10) with $i = H_2O$.

The study of methane steam reforming on rhodium has a steady literature basis. The analysis of methane SR experiments performed on Rh-based catalysts using a comprehensive and thermodynamically consistent micro-kinetic model [35,36] revealed that methane activation is the RDS and that all of the steps involving the co-reactant are quasi-equilibrated; consequently, methane activation is the sole kinetically relevant step. This is fully in line with the experimental findings of Wei and Iglesia [37,38] who verified the independence of CH_4 activation on the nature and the amount of the co-reactant.

Less broad is instead the literature on C_3H_8 steam reforming. Deutschmann et al. [21] have proposed a detailed reaction mechanism for ethane, propane, butane and natural gas steam reforming, in line with our experimental results, the authors found a global order lower than 1 for the kinetics of propane dissociation. Song et al. [39] also studied propane steam reforming on Rh (modified by addition of ceria and nickel), and found that data could be well explained by a Langmuir Hinshelwood kinetic expression, which incorporated the adsorption of propane and water and accounted for varying kinetic orders at varying temperature. Such kinetics seemed to be first order in the fuel at low C_3H_8 concentration.

Also in the steam reforming reaction CH_4 and C_3H_8 showed similar kinetic dependences, the estimate of the intrinsic kinetic constant of steam reforming is practically coincident with that of oxidation; this further supports the hypothesis that the rate

Table 3
Kinetic parameters for propane activation step.

	$k_{0, Ox}$ [mol/(cm^2 s atm)]	$E_{act, Ox}$ [kJ/mol]	$k_{0, SR}$ [mol/(cm^2 s atm)]	$E_{act, SR}$ [kJ/mol]
$C_3H_8 + 3Rh(s) \rightarrow 2CH_3(s) + CH_2(s)$	1.06E−05	30	1.80E−06	50
$C_3H_8 + 4Rh(s) \rightarrow CH_3(s) + 2CH_2(s) + H(s)$	1.06E−05	30	1.80E−06	50
$C_3H_8 + 5Rh(s) \rightarrow 3CH_2(s) + 2H(s)$	1.06E−05	30	2.10E−06	40

determining step of both reactions is related to C_3H_8 activation. The estimated activation energy amounted to 85 kJ/mol lower than that estimated for methane (92 kJ/mol), but higher than that of propane oxidation (80 kJ/mol).

4.3. Water gas shift

Pieces of evidence regarding the importance of the WGS reaction were provided by the steam reforming tests wherein the syngas composition and the CO/CO_2 ratio were controlled by the rate and by the reversibility of the WGS reaction. The SR experiments at varying C_3H_8 concentration (Fig. 9) showed a complete overlap of CO_2 production curves upon increasing the concentration of propane. This suggests that the forward WGS reaction was not strongly dependent on the concentration of CO (that increased with increasing C_3H_8 inlet concentration), but it mainly depends of the concentration of H_2O (that was maintained constant at 3%). The following expression is then proposed:

$$r_{WGS} = k_{WGS} \cdot P_{H_2O} \cdot (1 - \eta_{WGS}) \cdot \sigma_{CO} \tag{13}$$

The term $(1 - \eta_{WGS})$ and the term σ_{CO} account for the thermodynamic consistency of the equation and the activation of the reaction only in the presence of the co-reactant, respectively. Eq. (13) well agrees with the studies of Bunluesin et al. [40], who found a zero-order dependence on CO and first-order dependence on H_2O for ceria- and alumina-supported Rh catalysts.

Numerical analysis of CPO and steam reforming data pointed out that it is not possible to use one equation comprising both the direct and the reverse WGS steps. The direct and the reverse steps must be treated as two distinct reactions with different kinetic dependences and a coherent approach to the equilibrium. The following kinetic expression of RWGS was adopted, this is the same reported in the previous work on CH_4 CPO [29]:

$$r_{RWGS} = k_{RWGS} \cdot P_{CO_2} \cdot (1 - \eta_{RWGS}) \cdot \sigma_{H_2} \tag{14}$$

4.4. Methanation

CPO and SR tests clearly showed that at low temperature the formation of CH_4 accompanies to the formation of syngas (Figs. 3 and 6). It is well known in the literature that the methanation of CO and CO_2 occurs effectively on various transition metal catalysts [41–43]. The major indication from the experiments in annular reactor is that the kinetics of methane formation depends on H_2 partial pressure, but little on CO_x partial pressure, which is in line with the results reported in literature [44,45]. We note that under the conditions of the present study it is impossible to discriminate between a route of CO hydrogenation and route of CO_2 hydrogenation. For the sake of simplicity, we herein proposed a stoichiometry of methanation of CO and the following rate expression is proposed:

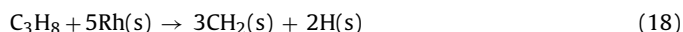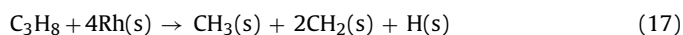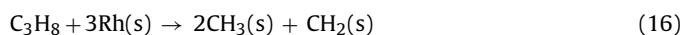$$r_{Met} = k_{Met} \cdot P_{H_2} \cdot (1 - \eta_{Met}) \cdot \sigma_{CO} \tag{15}$$

The term $(1 - \eta_{Met})$ and the term σ_{CO} account for the thermodynamic consistency of the equation and for the activation of the reaction only in the presence of the co-reactant, respectively. For Rh/Al_2O_3 catalysts, Vannice et al. [45] reported a kinetic equation having negative order (−0.2) for CO partial pressure and an order 1.05 for H_2 partial pressure. Differently from the results reported

by Vannice, a zero-order dependence on CO is introduced in Eq. (15), due to the lack of specific experimental indications. The estimated activation energy (30 kJ/mol) is not comparable with the values available in the literature (100 kJ/mol): this further support the simplifying character of the rate expression (15) and the need of further investigation.

4.5. A preliminary micro-kinetic analysis

The micro-kinetic analysis of the propane experiments is presently on-going. In previous studies [32,36], we developed a thermodynamically consistent micro-kinetic scheme for the description of CH_4 conversion over Rh catalysts. The kinetic model consists of 82 elementary reactions and 13 surface species and is capable of describing several processes, including CH_4 steam and dry reforming, partial oxidation, H_2 and CO combustion, WGS and its reverse. In this work, the micro-kinetic scheme was extended by adding lumped steps of C_3H_8 decomposition. A similar modeling approach of the adsorption of C_{2+} species has been adopted by Deutschmann and co-workers in the case of steam reforming of natural gas [21] and partial oxidation of iso-octane [20]. The adsorption step was modeled by assuming that higher hydrocarbons quickly lead to the formation of C* and H* species both via pyrolitic and oxy-pyrolitic routes. Even though such a rapid decomposition step represents a very simplified model, no evidence of catalytic production of C_2-C_{4+} species supported this assumption.

Differently from Deutschman et al., in this work, we explored the case that the dissociative adsorption of C_3H_8 occurred via the formation of CH_x intermediates (with $x \leq 3$), which react along the paths and kinetics of our C1 micro-kinetic scheme. The following stoichiometries were considered:

$$C_3H_8 + 3Rh(s) \rightarrow 2CH_3(s) + CH_2(s) \tag{16}$$

$$C_3H_8 + 4Rh(s) \rightarrow CH_3(s) + 2CH_2(s) + H(s) \tag{17}$$

$$C_3H_8 + 5Rh(s) \rightarrow 3CH_2(s) + 2H(s) \tag{18}$$

The C1-microkinetic scheme combined with the C_3H_8 activation step was incorporated in the model of the annular reactor, wherein for simplicity intraporous mass transfer limitations were neglected.

The following equation was used to describe the rate expression for C_3H_8 adsorption:

$$r = k_0 \cdot \exp\left[-\frac{E_a}{R}\left(\frac{1}{T} - \frac{1}{T_0}\right)\right] \cdot P_{C_3H_8} \cdot \theta_{Rh} \tag{19}$$

where $P_{C_3H_8}$ and θ_{Rh} are propane partial pressure and the coverage of Rh vacancies, respectively.

The kinetic parameters of Eq. (19) were adjusted to the experiments of C_3H_8 CPO tests in standard operating conditions and different sets of parameters were assumed for total oxidation and steam reforming regimes (Table 3). This simplification is coherent with the picture of a dissimilar distribution of surface coverage in total oxidation and steam reforming, thus, the assumption of coverage dependent parameters is reasonable. The oxygen limiting factor, σ_{O_2}, was used as indicator for switching from the total oxidation regime ($\sigma_{O_2} > 0$) to the steam reforming regime ($\sigma_{O_2} = 0$). The estimated values of the activation energies were taken as apparent activations energies, affected by the residual presence of intraporous resistances in the catalyst layer.
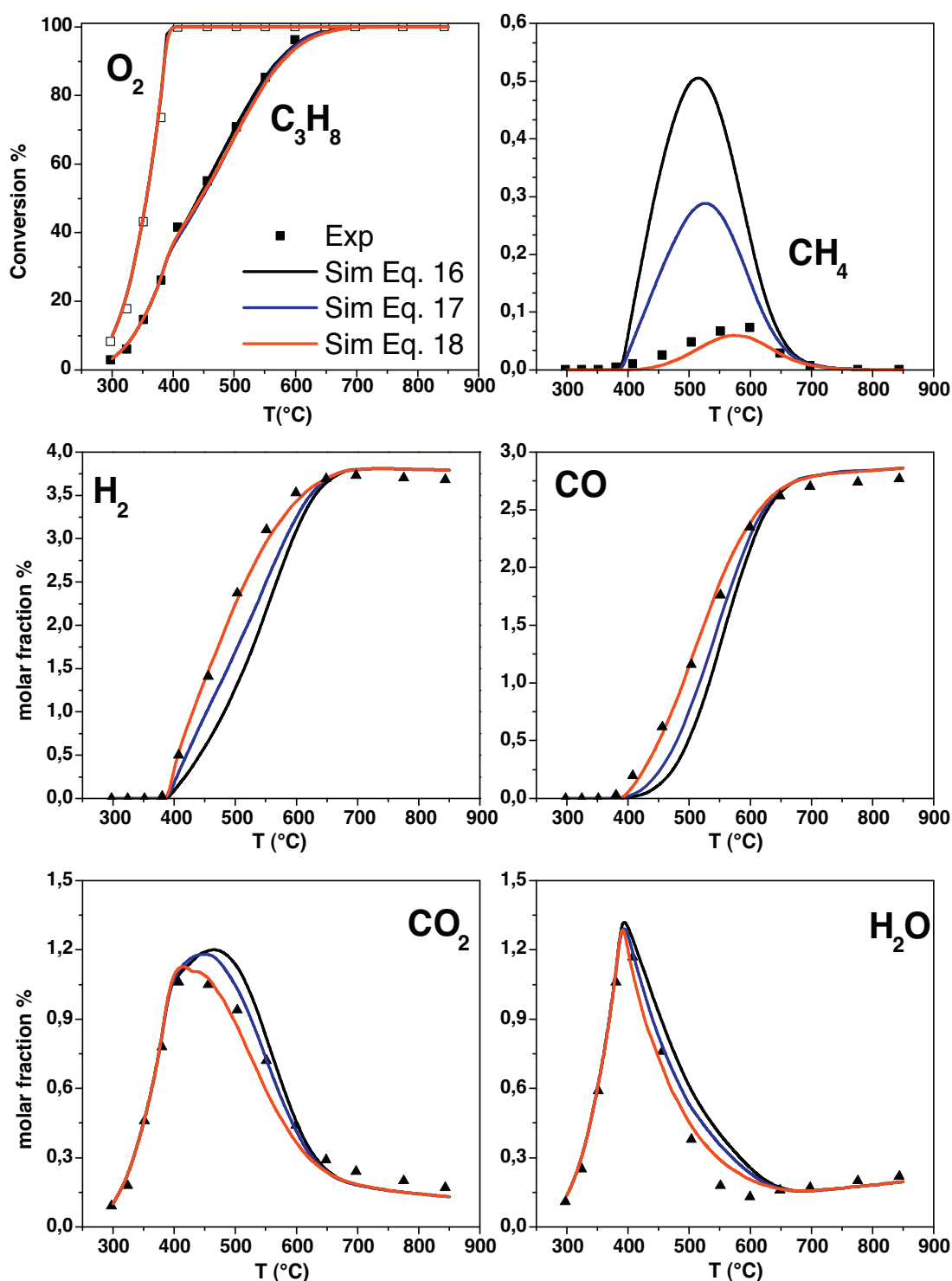
Fig. 10. Comparison between experimental data (symbols) and model predictions (solid lines) using the C_1 micro-kinetic scheme coupled with the proposed steps for C_3H_8 activation. Feed composition: $C_3H_8 = 1\%$, $O_2/C = 0.56$, N_2 to balance; GHSV $= 2 \times 10^6$ l(NTP)/kg$_{cat}$/h, atmospheric pressure.

Fig. 10 reports the experimental data and model simulations of conversion of reactants and molar fractions of products as a function of catalyst average temperature. The numerical analysis showed that the conversion of C_3H_8 and O_2 was well predicted by the model with all the three adsorption steps herein examined. On the opposite, the distribution of products was found to be strongly dependent on the stoichiometry of C_3H_8 activation. In particular, the prediction of CH_4 molar fractions is very sensitive to adsorption stoichiometry of C_3H_8: by considering an adsorption steps with

formation of $CH_3{}^*$ species (Eqs. (16) and (17)), the production of CH_4 was largely overestimated (from 3 to 5 times higher at 550 °C), while the agreement between model simulations and experimental data was very satisfactory in the case of $CH_2{}^*$ as the main intermediate of C_3H_8 decomposition (Eq. (18)). It is worth to recall that, according to our microkinetic scheme [36], the elementary steps of CH_4 dissociation in combination with pre-exponential factors and surface coverage are such that the rate determining step (RDS) of CH_4 reforming is the $CH_3{}^* \rightarrow CH_2{}^*$ step. Accordingly, the surface

enrichment of CH_3^* species increases the gas-phase concentration of methane more effectively than the enrichment of CH_x fragments with $x \leq 2$. This suggests that the formation of CH_x fragments ($x \leq 2$) is the rate determining step of C_3H_8 activation on Rh. This is a preliminary conclusion and the kinetic parameters need to be refined over wider experimental operating conditions.

5. Conclusions

The present work reports an extensive kinetic investigation of the catalytic partial oxidation of C_3H_8 over a 2 wt.% Rh/α-Al$_2$O$_3$ catalyst by using an annular microreactor. In the literature, a strong need exists for kinetic data of C_3H_8-CPO that are informative on the evolution of the process stoichiometry at increasing conversion of the fuel. As in the case of CH_4, also in the case of C_3H_8 we found that the intrinsic rates of fuel oxidation to CO_2 and H_2O and fuel reforming to CO and H_2 are comparable. However, these processes became consecutive in the CPO reactor because of an evident inhibiting effect of O_2 on steam reforming. Thus, CPO tests at low temperature were informative on the kinetics of C_3H_8 oxidation; CPO tests at high temperature and SR tests instead, informative on the kinetics of C_3H_8 reforming. From the numerical and the experimental analysis, the following conclusions can be drawn:

- Total oxidation and steam reforming of C_3H_8 showed a first-order dependence on fuel concentration and a zero-order dependence on the co-reactant concentration.
- Still, both oxidation and SR reactions exhibited overall kinetic orders lower than 1, apparently C_3H_8 total oxidation was moderately inhibited by H_2O adsorption while steam reforming was delayed in the presence of O_2 and influenced by the competitive adsorption of syngas.
- The analogies between oxidation of CH_4 and C_3H_8 suggested that the kinetic dependencies are direct consequences of surface coverage and hydrocarbon reactivity.
- WGS and RWGS had independent kinetics; WGS rate equation was found to be first order dependent on H_2O and independent of CO.
- At low temperature the formation of CH_4 accompanied to the formation of syngas, the kinetics of methane formation depended on H_2 partial pressure and little on CO_x partial pressure, but under the conditions of the present study it was impossible to distinguish between a route of CO hydrogenation and route of CO_2 hydrogenation. A simple rate equation for CO methanation with first order dependence on H_2 allowed to describe the data of methane production.
- Only at the highest temperatures, the activation of side gas-phase cracking reactions became significant with production of CH_4, C_2H_4 and C_3H_6.
- The preliminary micro-kinetic analysis of C_3H_8 confirmed that a good description of the measured conversion and product distribution can be obtained by assuming that the activation of propane mainly gives rise to the formation of surface CH_x fragments with $x \leq 2$.

Appendix A. Notation

x_i^B	bulk molar fraction of specie ith
x_i^W	wall molar fraction of specie ith
D_i	molecular diffusivity (m^2 s^{-1})
D_μ	microporous diffusivity (m^2 s^{-1})
D_M	macroporous diffusivity (m^2 s^{-1})
$D_{\text{eff},i}$	effective diffusivity (m^2 s^{-1})
z	axial coordinate (m)

z^*	dimensionless axial coordinate $z^* = z/d_h$
F_i	molar flow of species ith (mol s^{-1})
F_{TOT}^0	total inlet molar flow (mol s^{-1})
F_i^*	dimensionless molar flow of species ith $F_i^* = F_i/F_{TOT}^0$
R^*	aspect ratio $R^* = R_{\text{int}}/R_{\text{ext}}$
d_h	hydraulic diameter (m)
$Pe_{m,i}$	Péclet number $Pe_{m,i} = Re\,Sc_i$
υ	average gas velocity (m s^{-1})
Re	Reynolds number $Re = \upsilon d_h/\nu$
Sc_i	Schmidt number $Sc_i = \upsilon/D_i$
$K_{c,i}$	mass transfer coefficient (m s^{-1})
$Sh_{loc,i}$	local Sherwood number of species ith $Sh_{loc,i} = K_{c,i}d_h/D_i$
$z_{Sh,i}$	$z^*/Pe_{m,i}$
r_j	reaction rate (mol s^{-1} g^{-1})
P_i	partial pressure of the ith species (atm)
C_{TOT}	total concentration (mol m^{-3})
C_i^S	concentration at the catalyst wall of specie ith (mol m^{-3})
C_i^{eq}	equilibrium concentration at the catalyst wall of specie ith (mol m^{-3})
w_{cat}	catalyst weight (g)
S	geometrical surface area of the catalyst (m^2)

Greek symbols

ν	cinematic viscosity (m^{-2} s^{-1})
$\upsilon_{i,j}$	stoichiometric coefficient of the ith specie in the jth reaction
α_i	$w_{\text{cat}}d_hS^{-1}C_{TOT}^{-1}D^{-1}$
δ_L	thickness of the catalytic layer (m)
φ_i	generalized Thiele modulus of specie ith (–)
η_i^∞	effectiveness factor of specie ith at $\varphi \to \infty$
η_i	effectiveness factor of the ith
ε_M	macropore void fraction (–)
ε_μ	micropore void fraction (–)

References

[1] J.D. Holladay, J. Hu, D.L. King, Y. Wang, Catalysis Today 139 (2009) 244–260.
[2] J.N. Armor, Applied Catalysis A: General 176 (1999) 159–176.
[3] S.E.H. Brejc, Partial oxidation of hydrocarbons, in: H.S. Elvers, B. Ravenscroft, M. Rounsaville, J.F.G. Schultz (Eds.), Ullmann's Encyclopedia of Industrial Chemistry, VCH, New York, 1993.
[4] M. Maestri, A. Beretta, G. Groppi, E. Tronconi, P. Forzatti, Catalysis Today 105 (2005) 709–717.
[5] J. Warnatz, R.W. Dibble, U. Maas, Combustion, Physical and Chemical Fundamentals Modeling and Simulations, Springer, New York, 1996.
[6] E. Ruckenstein, H.Y. Wang, Journal of Catalysis 187 (1999) 151–159.
[7] M. Huff, P.M. Torniainen, L.D. Schmidt, Abstracts of Papers of the American Chemical Society 206 (1993) 127–130.
[8] B.C. Enger, J. Walmsley, E. Bjorgum, R. Lodeng, P. Pfeifer, K. Schubert, A. Holmen, H.J. Venvik, Chemical Engineering Journal 144 (2008) 489–501.
[9] B. Silberova, H.J. Venvik, J.C. Walmsley, A. Holmen, Catalysis Today 100 (2005) 457–462.
[10] T. Rostrup-Nielsen, Catalysis Today 106 (2005) 293–296.
[11] J.R. Rostrup-Nielsen, Journal of Catalysis 33 (1974) 184–201.
[12] J.B. Claridge, M.L.H. Green, S.C. Tsang, A.P.E. York, A.T. Ashcroft, P.D. Battle, Catalysis Letters 22 (1993) 299–305.
[13] M. Huff, L.D. Schmidt, Journal of Catalysis 149 (1994) 127–141.
[14] C.M. Balonek, J.L. Colby, L.D. Schmidt, AIChE Journal 56 (2010) 979–988.
[15] J.J. Krummenacher, K.N. West, L.D. Schmidt, Journal of Catalysis 215 (2003) 332–343.
[16] G.J. Panuccio, B.J. Dreyer, L.D. Schmidt, AIChE Journal 53 (2007) 187–195.
[17] R. Subramanian, G.J. Panuccio, J.J. Krummenacher, I.C. Lee, L.D. Schmidt, Chemical Engineering Science 59 (2004) 5501–5507.
[18] M. Hartmann, L. Maier, O. Deutschmann, Applied Catalysis A: General 391 (2011) 144–152.
[19] L. Maier, M. Hartmann, S. Tischer, O. Deutschmann, Combustion and Flame 158 (2011) 796–808.
[20] M. Hartmann, L. Maier, H.D. Minh, O. Deutschmann, Combustion and Flame 157 (2010) 1771–1782.
[21] B.T. Schadel, M. Duisberg, O. Deutschmann, Catalysis Today 142 (2009) 42–51.
[22] D. Livio, A. Donazzi, A. Beretta, G. Groppi, P. Forzatti, Industrial and Engineering Chemistry Research 51 (2012) 7573–7583.
[23] A. Donazzi, D. Livio, M. Maestri, A. Beretta, G. Groppi, E. Tronconi, P. Forzatti, Angewandte Chemie International Edition 50 (2011) 3943–3946.
[24] A. Donazzi, D. Livio, A. Beretta, G. Groppi, P. Forzatti, Applied Catalysis A: General 402 (2011) 41–49.
[25] A. Beretta, A. Donazzi, D. Livio, M. Maestri, G. Groppi, E. Tronconi, P. Forzatti, Catalysis Today 171 (2011) 79–83.
[26] T. Bruno, A. Beretta, G. Groppi, M. Roderi, P. Forzatti, Catalysis Today 99 (2005) 89–98.
[27] W. Ibashi, G. Groppi, P. Forzatti, Catalysis Today 83 (2003) 115–129.
[28] A. Beretta, T. Bruno, G. Groppi, I. Tavazzi, P. Forzatti, Applied Catalysis B: Environmental 70 (2007) 515–524.
[29] A. Donazzi, A. Beretta, G. Groppi, P. Forzatti, Journal of Catalysis 255 (2008) 241–258.

[30] A. Donazzi, A. Beretta, G. Groppi, P. Forzatti, Journal of Catalysis 255 (2008) 259–268.
[31] http://navier.engr.colostate.edu/~dandy/code/code-4/index.html
[32] M. Maestri, D.G. Vlachos, A. Beretta, G. Groppi, E. Tronconi, AIChE Journal 55 (2009) 993–1008.
[33] A.B. Mhadeshwar, J.R. Kitchin, M.A. Barteau, D.G. Vlachos, Catalysis Letters 96 (2004) 13–22.
[34] M. Garcia-Diéguez, Y.H.C. Chin, E. Iglesia, Journal of Catalysis 285 (2012) 260–272.
[35] M. Maestri, D.G. Vlachos, A. Beretta, P. Forzatti, G. Groppi, E. Tronconi, Topics in Catalysis 52 (2009) 1983–1988.
[36] M. Maestri, D.G. Vlachos, A. Beretta, G. Groppi, E. Tronconi, Journal of Catalysis 259 (2008) 211–222.

[37] J.M. Wei, E. Iglesia, Journal of Catalysis 225 (2004) 116–127.
[38] J.M. Wei, E. Iglesia, Journal of Catalysis 224 (2004) 370–383.
[39] Y. Li, X. Wang, C. Xie, C. Song, Applied Catalysis A: General 357 (2009) 213–222.
[40] T. Bunluesin, R.J. Gorte, G.W. Graham, Applied Catalysis B: Environmental 15 (1998) 107–114.
[41] R.P. Underwood, C.O. Bennett, Journal of Catalysis 86 (1984) 245–253.
[42] M. Marwood, R. Doepper, A. Renken, Applied Catalysis A: General 151 (1997) 223–246.
[43] P. Panagiotopoulou, D.I. Kondarides, X.E. Verykios, Journal of Physical Chemistry C 115 (2011) 1220–1230.
[44] A. Erdohelyi, J. Cserenyi, F. Solymosi, Journal of Catalysis 141 (1993) 287–299.
[45] M.A. Vannice, Journal of Catalysis 50 (1977) 228–236.